# Investigation on The Flow Characteristics of Rotating Nozzle Cavitation Water Jet Flow Field

W. Wu[1], Y. Xu[1,2†], Y. Yan[1,2], S. Li[1,2], J. Zhang[1,2] and Z. Wang[1,2]

[1] *Mechanical Scientific and Engineering College of Northeast Petroleum University, Daqing, Heilongjiang Province, 163318, China*
[2] *Daqing Oilfield Production Engineering & Research Institute, Daqing, Heilongjiang Province, 163453, China*

*†Corresponding Author Email: xuyanzhf@nepu.edu.cn*

## ABSTRACT

Rotating cavitation water jet technology is widely used in many industrial fields such as pipeline cleaning, unblocking, cutting, etc. To more accurately analyse the flow characteristics of rotating cavitating water jets, the specific impact of the nozzle rotational velocity on the evolution of the whole flow field was systematically explored in this work. More specifically, a numerical simulation study of a three-nozzle rotating cavitation nozzle was carried out using the Large Eddy Simulation method of the WALE sub-lattice model. After determining 12MPa as the inlet pressure condition. The tangential velocity, vorticity, cavitation cloud development patterns, and wall pressure changes in the internal flow field at different rotational speeds were compared. From our analysis, it was demonstrated that as the nozzle rotates faster, the tangential velocity of the jet increases, leading to a deflection of the jet. The degree of deflection is positively related to the rotational speed. Under the action of shear, the vortex structure will gradually increase in size as the jet develops and finally breaks up and disintegrates. The period of cavitation cloud development and maximum volume fraction increases with increasing the rotational speed; When the rotational speed increases, the striking pressure of the rotating jet on the wall first increases and then decreases. The fitted jet curve can better reproduce the jet development pattern. The derived fitting formula allows the determination of the corresponding impact angle according to the magnitude of the rotational velocity. The existence of a higher nozzle rotation speed induces a greater curvature of the fitted curve, the deflection angle, and the impact angle. Our work provides a robust theoretical reference for the field application of the rotating nozzle cavitation water jet technology and can be used as technical support for industrial well-bore unblocking and pipeline descaling.

## 1. INTRODUCTION

Pipework is an integral part of many industrial processes. Numerous piping structures exist in the food, chemical, power, and petroleum industrial sectors. A nozzle combining rotation and cavitation has been discovered and widely used to solve various internal pipe work problems. For instance, using the huge instantaneous pressure and strong destructive force generated at the moment of bubble collapse combined with the full-coverage characteristics of nozzle rotation, Guo et al. (2018) reported a better operating efficiency.

Peng et al. (2018) conducted a visual erosion test of the cavitation jet flow field. The spatio-temporal distribution of the cavitation clouds was analysed, and the morphology of the eroded samples was analysed from both macroscopic and microscopic perspectives. The descaling and erosion capability of the cavitation water jets was also demonstrated. In another interesting work, Cai et al. (2020) found that the erosion characteristics of the cavitation effects are affected by a number of factors, such as fluid parameters (fluid pressure, cavitation number, etc.), ambient temperature, geometry of the test setup, etc. Thus, the generation of different jet frequencies can inhibit or promote pressure oscillations in the self-excited state, which can accelerate the development cycle of the cavitation clouds. Dabiri et al. (2010) investigated the development of bubbles within cavitation effects in

| NOMENCLATURE | | | |
|---|---|---|---|
| $D_s$ | cavitation nozzle inlet diameter | $L_4$ | diffusion segment length |
| $L_1$ | cavitation nozzle inlet length | $L$ | jet core curve |
| $D_x$ | diameter of resonant cavity | $w$ | sample points of the jet curve |
| $L_2$ | resonant cavity length | $a$ | tangent line at w |
| $d$ | throat diameter | $\alpha$ | angle of impact |
| $L_3$ | throat length | $b$ | sample point w in line with the start of the jet |
| $\theta$ | diffusion angle | $\beta$ | angle of divergence |
| $D$ | deflection distance | $R$ | jet radius |
| $L_0$ | starting deflection distance of jet | $B_1 、 B_2$ | jet Curve Fitting Coefficient |
| $A$ | tangent-line equation | $A_0$ | tangent slope |
| $\alpha_0$ | tangent line origin | $x$ | nozzle rotation speed |

shear and extended flows. The three-dimensional behaviour of the cavitation bubbles during growth to collapse was observed by solving the Navier-Stokes equations. It was found that when the vacuole collapses, the interaction between the vacuole and the internal flow field leads to the generation of re-entrant jets on both sides of the cavitation bubble. Due to viscosity, surface tension, and shear, the re-entrant jet has sufficient strength to break the large bubbles into smaller ones. Wu et al. (2022) carried out a flow field characterization of organ-pipe cavitation nozzles and pointed out that the effectiveness of cavitation is mainly affected by the size of the throat cross-section. The latter reaches its maximum length and volume when the length of the throat section is twice the diameter of the throat.

Wang et al. (2023a) used cavitation jets in conjunction with rotatable nozzles and found that it was difficult to directly observe due to the large perturbations and phase changes in the flow field of the rotating nozzles. The authors suggested that numerical simulation methods should be used to further investigate this effect. The computational method of Large Eddy Simulations was proposed by Smagorinsky (1963) and is now mostly used to simulate atmospheric airflow. Large eddy simulation is performed by dividing the eddy structure into large and small scales through a low-pass filter. Large-scale vortex structures are directly solved in the calculations, while small-scale vortex structures need to be simulated with a sub-lattice model. (Wang & Ostoja-Starzewski, 2005); (Bensow & Bark, 2010) found that this model can predict the cavitation effects more accurately. Particularly, Wang et al. (2023b) used three sub-lattice models, namely the SM model, the WALE model, and the WMLES model, to simulate the large vortices of organ-pipe cavitation nozzles. The applicability of the different sub-lattice models for simulating and investigating the flow field within the cavitation water jet and the mechanism of the cavitation water jet were investigated. It was concluded that the WALE model can simulate the cavitation cloud evolution cycle more accurately and capture a larger number of small-scale eddies. Yu et al. (2022) numerically simulated the Clark-Y small-scale vane grating using the Large Eddy Simulations method, and deeply investigated the basic mechanism of the periodic evolution of cavitation-vortex interaction in the U-shaped cavity. The formation principles of the high-pressure and low-velocity zones were perfectly explained using kinetic processes. Combining vortex kinematics and the re-entrant jet theory,

the dynamic evolution mechanism of the cavitation clouds and cavitation bubbles in the flow field inside a U-shaped cavity can be obtained. Ji et al. (2017) also investigated the phenomenon of cavitation attached to the turbulent surface of hydrofoils by using a combination of Large Eddy Simulations and a homogeneous cavitation model. From the predictions of the cavitation vapour phase volume fractions and lift coefficients obtained from the simulations, the periodic nature can be clearly seen. In addition, the simulated predictions are consistent with the experimental data parameters. At the same time, the transient behavioural characteristics of the non-constant vacuole evolutionary dynamics (vacuole incipience, development, shedding, collapse) can be accurately captured. By comparing the cavitation cloud vapour phase volume fraction and time-frequency domain periodicity obtained from the LES model calculations, Bhatt and Mahesh (2019) found that the cavitation cloud morphology is very similar to the experimental shots. The shedding periodicity frequency and cavitation shock wave propagation velocity are in direct agreement with the experimental results. Meanwhile, the simulation approach allows a better identification of the cavitation in cross-directional vortices in the shear region. It was observed that the cavitation bubbles mainly occur in the shear layer, intermittently in the cavity, and during the bubble shock cycling process.

Li et al. (2023) proved that the rotational speed contributes to some extent to the cavitation effect. For rotary cavitation of the modified lobe type, the high rotational speed induces the generation of longer and larger vacuoles by the cavitation, resulting in a more pronounced cavitation effect. The surface area and volume of the cavitation bubbles are continuously increasing with the increase of the rotational speeds. Ni (2022) reported that changes in the nozzle's rotational velocity have a direct impact on the angle of incidence of the jet impact. The rotating nozzle avoids the "Water Cushion Effect" caused by the continuous jet at a fixed impact angle. The peak wall affects the pressure distribution and leads to a slight increase in the wall shear pressure over a certain speed range. As the speed continues to increase, the pressure and shear will begin to decrease due to the energy loss. Using an improved separation vortex simulation method and shear stress transport equation, Chen et al. (2020) systematically analysed the development and evolution of the vortex structure, the change characteristics of the velocity field pressure field, and the

turbulence pulsation fluctuation law inside the rotating jet flow field. The simulated results showed that the development of cavitation water jet vortex periodic structure is grouped into three evolutionary stages. Moreover, the rotating flow action can significantly enhance the radial turbulent pulsation, and increase the jet diffusion angle and turbulent pulsation. Wang et al. (1999) investigated the structural characteristics of rotating jets, as well as the distribution of the flow field. The authors demonstrated that the rotating jets possess three-dimensional velocities, which result in a larger impact area. Various tests in the literature have also shown that the efficiency of rotating jets in breaking up rock drilling is much higher than that of ordinary round jets. Particularly, Zhao et al. (2023) used the rotating abrasive water jet for cutting oil pipelines within an oil field and simulated the flow characteristics of the flow field within the cutting process. In parallel, the authors analysed the conditions under which the operating parameters affect the industrial cutting operation, and optimised them. It was found that two vortices with opposite directions were formed on both sides of each nozzle of the internal flow field in the range of 360∘. When the spacing was less than 7 mm, a larger standoff distance induced a higher pressure reaching the wall, and a better cutting effect of the rotating nozzle. Zhao et al. (2020) combined cavitation and rotation to design a polishing nozzle for low-pressure conditions. The effectiveness of the rotating cavitation nozzle was verified based on the abrasive flow simulation method of Computational Fluid Dynamics (CFD) and the monocrystalline silicon wafer polishing test. The nozzle was also analysed to find differences with the conventional operating process of polishing by low pressure abrasive jetting. It was proven that the operational efficiency of the rotary cavitation nozzle was higher than that of the traditional abrasive jet. Xu (2022) utilized rotary cavitation water jet technology for oil well decommissioning, combining 90° and rotary nozzles with shaped two-chamber Helmholtz nozzles, and optimising the design of nozzle geometry construction, which increased the jet velocity of the nozzles by 3.508 m/s.

From the above-mentioned analysis, it can be seen that the rotational action can effectively increase the erosive capacity of the jet. However, the underlying flow mechanism and dynamic properties of the flow field within the jet under the joint action of the rotation and cavitation effects have been scarcely reported. Along these lines, in this work, the Large Eddy Simulations method was adopted to numerically simulate the cavitation jet flow field of a submerged rotating nozzle used in industrial pipeline cleaning and unblocking conditions.

## 2. MODEL INTRODUCTION

### 2.1 Geometric Structure Parameters

The organ-pipe cavitating nozzle size has been optimized in the literature, and its structure is shown in Fig. 1. The main structural dimensions are: Inlet diameter of $D_s$=6.4 mm. Inlet length of $L_1$=5 mm. Diameter of the resonant cavity of $D_x$=3.2 mm. Resonant Cavity Length of $L_2$=5.2 mm. Throat diameter of $d$=1 mm. Throat length of $L_3$=1 mm. Diffusion angle $\theta$ = 25°. Diffusion segment
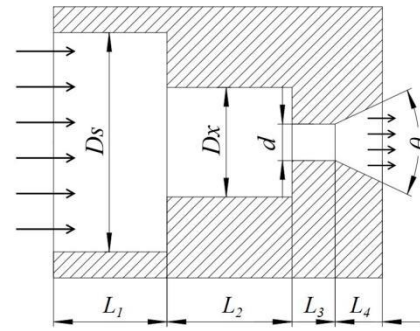


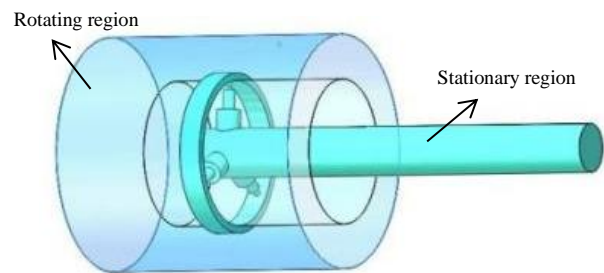**Fig. 1 Schematic diagram of organ-pipe section dimensions**



**Fig. 2 Schematic diagram of the fluid calculation domain of the rotating nozzle**

length of $L_4$=1.5 mm. The arrows indicate the direction of the incoming flow, which flows through $L_1$, $L_2$, $L_3$, $L_4$ successively.

The focus of this work is on the evolution of the rotating field and the formation process of the cavitation cloud after the rotation effect is superimposed on the cavitation nozzle. The simplified fluid domain obtained by removing the connection part of the nozzle to the motor during the modelling process is depicted in Fig. 2. The fluid domain is defined as two parts, namely the rotating region and the stationary region. The rotary nozzles contain three organ-pipe cavitating nozzles. The inlet was extended by a short distance to ensure the full development of the jet and reduce the influence of the inlet on the core region of the flow field. After conducting the dimensionless treatment, the outflow field diameter to throat (d) ratio was 62. The jet is mainly developed in the radial direction, centred on the core region of the jet, and extended by the same distance in both directions of the axis to ensure that the jet is not affected.

### 2.2 Flow Field Meshing

According to the mesh diagram drawn by the ICEM software, when the rotating nozzle is in operation, the three nozzle sections of the nozzle body are in the rotating region, while the external flow field region is at rest. Therefore, the mesh is defined as two regions, namely the outflow field rotation area and the inflow field stationary area, which will facilitate the drawing of the mesh. These two areas transfer data through the interface. Large The Eddy Simulations have high mesh requirements for the encryption of the mesh. To save computational resources, local encryption and boundary layer encryption were used,

**Table 1 Comparison of the vapour phase volume fractions in different meshes**

|  | Number（$10^6$） | Maximum vapour phase volume fraction | Surface-averaged vapour phase volume fraction |
|---|---|---|---|
| Mesh1 | 1.73 | 0.902 | 0.0073 |
| Mesh2 | 2.66 | 0.907 | 0.0078 |
| Mesh3 | 2.99 | 0.908 | 0.0116 |
| Mesh4 | 3.65 | 0.907 | 0.0117 |
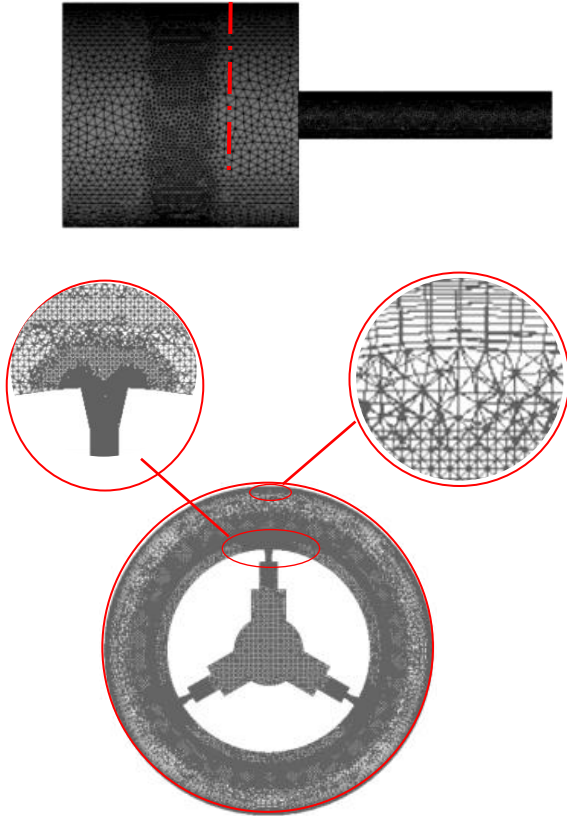


**Fig. 3 Schematic diagram of the jet core surface meshes**

with boundary layer encryption for the near-wall mesh and local encryption for the core region where the water jets develop. Additionally, density box encryption for the cylindrical and diffusive portions of the three organ pipe nozzles, as well as the region of large gradients, were adopted. The first grid height of the boundary layer was 0.08 mm, the variation rate was 1.1, and 15 layers were encrypted. The Y+-values on the core were clustered around 5. Mesh-independent studies were performed on these four sets of meshes, and the total number of meshes was 1.73 million, 2.66 million, 2.99 million, and 3.65 million, respectively. The inlet condition selects the pressure inlet, and the value was set to 12 MPa. The outlet parameter condition was set to the pressure outlet, and the value was set to 101325 Pa. The time step required for the calculation was specified as $1\times10^{-5}$ s, and the simulation results are listed in Table 1. From our analysis, it was found that the maximum gas-phase volume fraction parameter and the core surface average gas-phase volume fraction values increased with the number of meshes. When the number of meshes was increased to 2.66 million, the maximum change in the vapour phase volume

fraction by increasing the number of meshes was less than 1%. When the number of meshes was 2.99 million, the surface-averaged vapour-phase volume fraction by increasing the number of the meshes was less than 1%. The third set of 2.99 million meshes was selected for the subsequent simulation under the premise of combining the above two reference quantities and fully considering the computational resources, and its computational domain meshes are displayed in Fig. 3.

## 3. CALCULATION MODELS AND METHODS

### 3.1 Mixture Model Control Equations

The flow field with cavitation contains the two-phase flow of vapour and liquid. Therefore, a multi-phase flow model needs to be added to the simulation of the rotating cavitation water jet flow field. The mathematical equations of the continuity and momentum under the mixture model setting are:

$$\frac{\partial}{\partial t}\left(\rho_m\right)+\nabla\cdot\left(\rho_m\vec{v}_m\right)=0 \tag{1}$$

$$\frac{\partial}{\partial t}\left(\rho_m\vec{v}_m\right)+\nabla\cdot\left(\rho_m\vec{v}_m\vec{v}_m\right)=-\nabla p+\nabla\cdot\left[\mu_m\left(\nabla\vec{v}_m+\nabla\vec{v}_m^T\right)\right]$$
$$-\nabla\cdot\left(\sum\alpha_K\rho_K\vec{v}_{dr,k}\vec{v}_{dr,k}\right)+\rho_m\vec{g}+\vec{F} \tag{2}$$

$\vec{v}_m$ is the mass average velocity (m/s) calculated by the following formula:

$$\vec{v}_m = \frac{\sum_{k=1}^{n}\alpha_k\rho_k\vec{v}_k}{\rho_m} \tag{3}$$

$\rho_m$ denotes the mixed density (kg/m³) calculated by following the formula:

$$\rho_m = \sum_{k=1}^{n}\alpha_k\rho_k \tag{4}$$

$n$ refers to the total number of the fluid media (two phases are included in this study); $\vec{F}$ stands for volumetric forces; $\mu_m$ is the viscosity of the mixture calculated by the formula:

$$\mu_m = \sum_{k=1}^{n}\alpha_k\mu_k \tag{5}$$

$\vec{v}_{dr,k}$ states the slip velocity of the $k$ phase:

$$\vec{v}_{dr,k} = \vec{v}_k - \vec{v}_m \tag{6}$$

$\alpha_k$ represents the volume fraction of the $k$ phase.

## 3. 2 Control Equations for Large Eddy Simulations

The ANSYS FLUENT 2021R2 software package was used for the simulations. The Large Eddy Simulations can distinguishe the vortex motion of a turbulent body into large-scale eddies and small-scale eddies by means of a filter function. The continuity and momentum equations were obtained after filtering:

$$\frac{\partial \rho}{\partial t} + \frac{\partial}{\partial x_i}(\rho \bar{u}_i) = 0 \tag{7}$$

$$\frac{\partial}{\partial t}(\rho \bar{u}_i) + \frac{\partial}{\partial x_j}(\rho \bar{u}_i \bar{u}_j) = -\frac{\partial \bar{p}}{\partial x_i} + \frac{\partial}{\partial x_j}\left(\mu \frac{\partial \bar{u}_i}{\partial x_j}\right) - \frac{\partial \tau_{ij}}{\partial x_j} \tag{8}$$

$\rho$ is the density of the fluid medium (kg/m³); $\bar{u}_i$ and $\bar{u}_j$ are the directional velocities of the fluid (m/s); $\bar{p}$ denotes the hydrostatic pressure (Pa); $\tau_{ij}$ refers to sub-lattice scale stress whose formula is:

$$\tau_{ij} = -2\mu_t \bar{S}_{ij} + \frac{1}{3}\tau_{kk}\delta_{ij} \tag{9}$$

## 3. 3 Wall Adapted Local Eddy Viscosity (WALE) Model Eddy Viscosity Equation

The accuracy of large eddy simulation results is affected by the sub-lattice equations. The sub-lattice models that are currently widely used in large eddy simulations are the Smagorinsky-Lilly Model, Wall-Applied Localised Vortex Adhesion Model, and the Algebraic Wall Model. According to the literature, it has been found that the Wall-Applied Localised Vortex Adhesion Model is better than the other two sub-lattice models in simulating the cavitation jet flow field.

The Wall-Applied Localised Vortex Adhesion Model is as follows:

$$\mu_t = \rho L_s^2 \frac{\left(S_{ij}^d S_{ij}^d\right)^{\frac{3}{2}}}{\left(\bar{S}_{ij}\bar{S}_{ij}\right)^{\frac{5}{2}} + \left(S_{ij}^d S_{ij}^d\right)^{\frac{5}{4}}} \tag{10}$$

$L_s$ and $S_{ij}^d$ takes its value through the following formula:

$$L_s = \min\left(kd, C_w V^{\frac{1}{3}}\right) \tag{11}$$

$$S_{ij}^d = \frac{1}{2}\left(\bar{g}_{ij}^2 + \bar{g}_{ji}^2\right) - \frac{1}{3}\delta_{ij}\bar{g}_{kk}^2, \bar{g}_{ij} = \frac{\partial \bar{u}_i}{\partial x_j} \tag{12}$$

$C_w$ is a WALE constant that takes the value of 0.325.

## 3.4 Zwart-Gerber-Belamri（ZGB）Mathematical Cavitation Modelling Equations:

The Zwart-Gerber-Belamri cavitation model is as follows:

When $P \leq P_V$,

$$R_e = F_{vap}\frac{3\alpha_{nuc}(1-\alpha_v)\rho_v}{\Re_B}\sqrt{\frac{2(P_V - P)}{3\rho_l}} \tag{13}$$

When $P \geq P_V$,

$$R_c = F_{cond}\frac{3\alpha_v\rho_v}{\Re_B}\sqrt{\frac{2(P - P_v)}{3\rho_l}} \tag{14}$$

$P$ is the localised pressure; $P_v$ is the saturated vapour pressure; $\Re_B$ takes the value of $10^{-6}m$ for the radius of the bubble; $\alpha_{nuc}$ takes the value of $5 \times 10^{-4}$ for the bubble volumetric fraction; $F_{vap}$ takes the value of 50 for the evaporation coefficient of liquids; $F_{cond}$ takes the value of 0.01 for the condensation factor; $\rho_l$ denotes the phase density of liquid; $\rho_v$ states the vapour phase pressure.

## 3. 5 Boundary Conditions and Discretisation Methods

This work focused on the impact of the rotational speed variations on the development of velocity, vorticity, and cavitation cloud development patterns in the flow field. These variations were numerically calculated using FLUENT software. The pressure inlet was determined using a value of 12 MPa and the outlet pressure using a value of 101325 Pa, eliminating the sliding wall. The medium was fresh water at a temperature value of 25° C with a saturated vapour pressure of 3169 Pa. Its density and viscosity were 1000 kg/m³ 0.89 mPa·s, respectively. To enhance the accuracy of the calculation results during the large eddy simulations, the stable flow field was first obtained by the k-e model, which was used as the initial flow field for the calculations. Then, the large eddy model was turned on, the WALE model in the Large Eddy Simulation sub-lattice model was selected, and a velocity-pressure coupling algorithm was used. Bounded Second Order Implicit formulation was chosen for the mathematical transient term equation and PRESTO! format discrete formulation was designated as the pressure term equation. The time step was set to $10^{-5}$ s. Each time step was iterated 20 times and the convergence accuracy of the residuals was set by the continuous term Continuity to 0.00001. The rotation speed was set variable by using a sliding mesh.

### 3.6 Sliding Meshes Model

When simulating the rotating cavitation water jet flow field, the nozzle area was in the state of rotating motion, and the flow field outside the nozzle was in the static state. Hence, it involved the dynamic and static interference problem, whereas the simulation of the dynamic and static
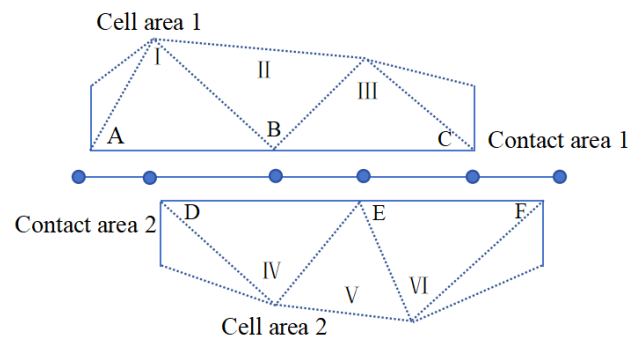
**Fig. 4 Schematic diagram of data transfer for Sliding Meshes Model**

interference problem mainly relies on the Dynamic Meshes and Sliding Meshes Models. The motion of the boundary of the dynamic meshes can be defined in two ways. More specifically, one is predefined by UDF (User Defined Function), and the other is not predefined, and its motion is determined by the results of the previous calculation. Both of these ways involve re-demarcation of the mesh, which may lead to a lower quality or even a negative volume mesh. However, this could in turn lead to non-convergence of the computation. Compared with the dynamic mesh, the sliding mesh does not involve a mesh reorganization problem, saves computational resources, and the calculation results are more stable. For this reason, in this work, the sliding mesh for simulation calculation was adopted.

In the simulation process with the increase of the time step length of the motion domain in accordance with its own speed of movement to produce displacement, in the process of the motion domain and the stationary domain of the respective interface with the calculation of the formation of a new information interface in each time step, through fluxes on interface to achieve the information transfer between the motion domain and the stationary domain of the flow field in each time step. The schematic diagram of the slip mesh data transfer is shown in Fig. 4.

The conservation equation is as follows:

$$\frac{d}{dt}\int_V \rho\phi dV + \int_{\partial V} \rho\phi\left(\vec{u}-\overrightarrow{u_g}\right)\cdot d\vec{A} = \int_{\partial V} \Gamma\nabla\phi\cdot d\vec{A} + \int_V S_\phi dV \quad (15)$$

where $\vec{u}$ is the velocity vector, $m/s$; $\overrightarrow{u_g}$ denotes the mesh movement speed, $m/s$; $\Gamma$ states the diffusion coefficient; $S_\phi$ signifies the source term for $\phi$.

From the above conservation equation, it can be seen that the mesh motion in the slip mesh is rigid and its mesh volume does not change with time, which can be calculated as follows:

$$V^{n+1} = V^n \quad (16)$$

**3.7 Experimental Verification**

In this work, a high-speed camera test of a rotating cavitation water jet in a restrained pipe under stationary conditions was carried out to verify the accuracy of the large vortex simulation method in comparison with the numerical simulation results. One of three nozzles was selected to track the evolutionary pattern of the cavitation cloud development over a cycle (Fig. 5). Photographs were taken at fixed intervals of 0.1 ms using a high-speed camera under experimental conditions of 5 MPa. The numerical simulation time step was $10^{-5}$. By comparing the developmental patterns of the experimental and the simulated cavitation clouds, it was revealed that their periodicity is disturbed by circumferential constraints, with the cavitation cloud affecting the tube wall before shedding. From the development period, it was observed that the experimental cavitation cloud breaks between 0.4 ms and 0.5 ms, while the simulated cavitation cloud affects the tube wall and breaks at 0.46 ms. This effect suggests that the simulated and experimental results are in

good agreement. Thereby, the proposed numerical simulation method can be used in the work of the flow field characteristics of rotating cavitating water jets.
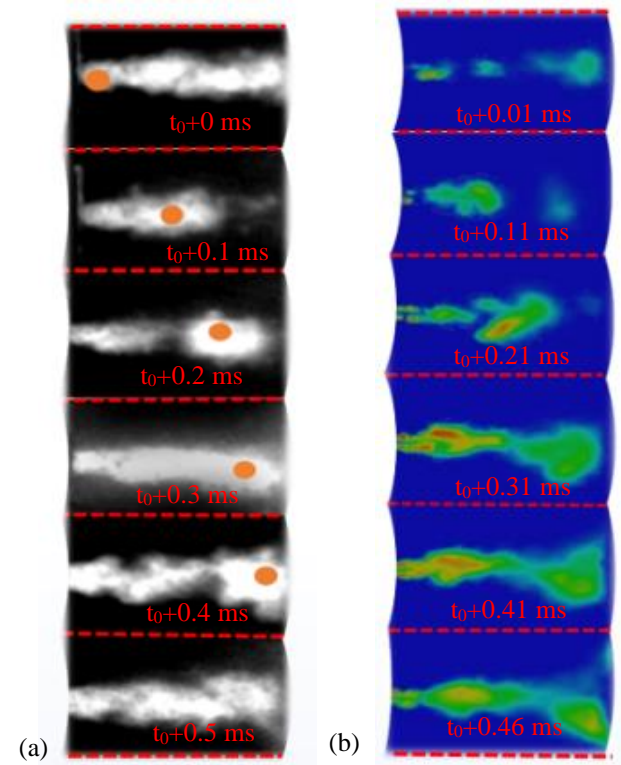


**Fig. 5 Comparison of the experimental and simulated cloud images**

**4. ANALYSIS OF RESULTS**

**4.1 Analysis of the Effect of Inlet Pressure on Cavitation Jets**

In order to investigate the cavitation cloud evolution law between the nozzle outlet and the wall flow field under different pressure conditions, the inlet pressures were set to 5 MPa, 8 MPa, 12 MPa and 15 MPa, respectively. The numerical simulation study meets the continuous term residual accuracy of $10^{-5}$, and the simulation results are considered to be stable. A single nozzle was selected to track the growth process of the cavitation cloud from incipient to collapsed when the rotational speed was 0. It was found that the cavitation phenomenon was generated in the diffusion section of the throat and formed stable cavitation bubbles. After the jet is ejected for viscous effect to generate velocity difference with the surrounding fluid, the reverse pressure difference effect occurs, which makes the cavitation bubbles behave as gradually increasing shear cavitation clouds in the flow field. Pressure in the 5-12 MPa conditions cavitation cloud development is manifested in four stages incipient, development, shedding, collapse. When the cavitation cloud develops to $t_0+240$ μs, the cavitation cloud is completely collapsed at 5 MPa, the 8 MPa cavitation cloud is just starting to undergo collapse, and the 12 MPa
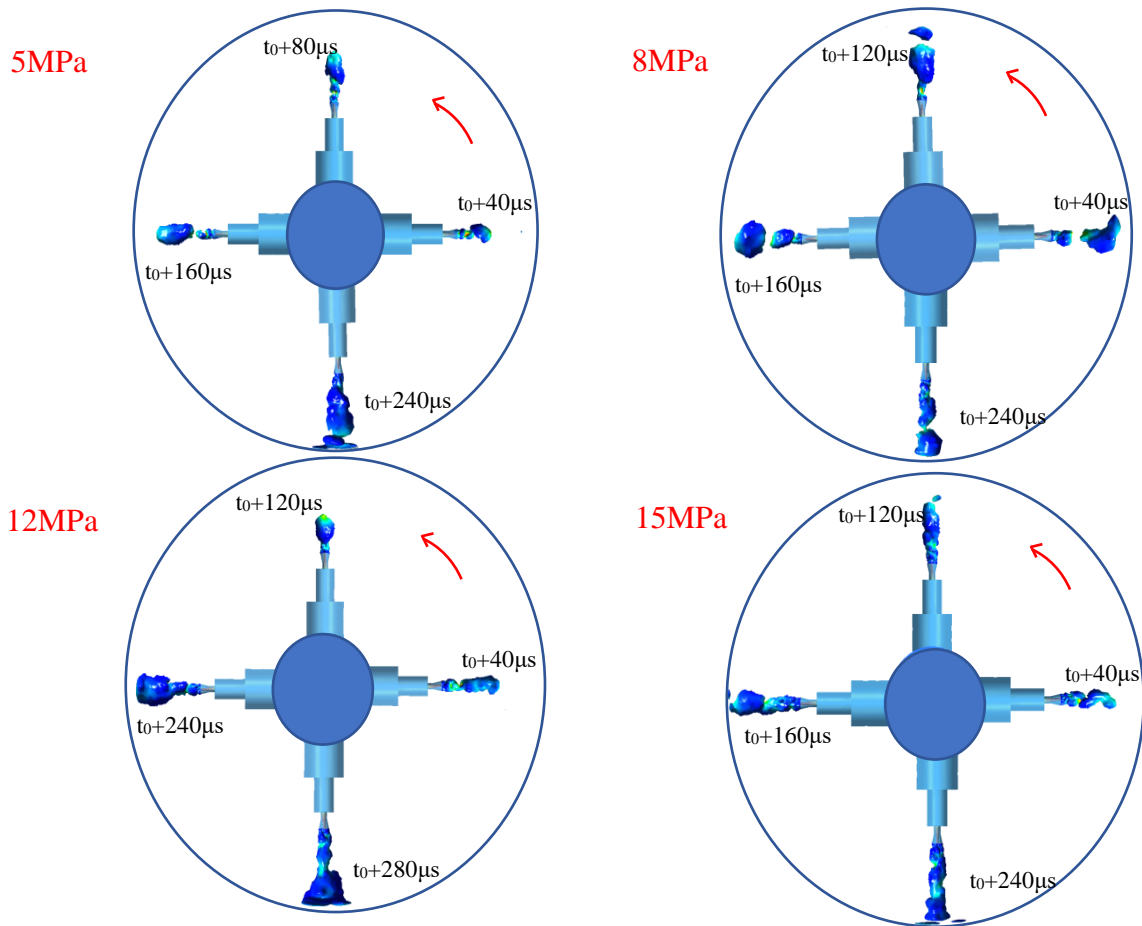
**Fig. 6 Cavitation cloud development diagram at different pressures**

**Table 2 Table of values of velocity, meteorological volume fraction and wall pressure at different inlet pressures after time averaging**

| Inlet pressure condition | Maximum velocity（$10^2$） | Maximum vapour phase volume fraction | Maximum pressure at wall surface（$10^6$） |
|---|---|---|---|
| 5Mpa | 1.03 | 0.893 | 0.74 |
| 8Mpa | 1.3 | 0.906 | 1.28 |
| 12Mpa | 1.59 | 0.927 | 2.05 |
| 15Mpa | 1.78 | 0.908 | 2.61 |

cavitation cloud is in the development stage. When the inlet pressure increases to 15 MPa, the cavitation cloud strikes the wall after two stages of incipient and development, and collapse occurs as shown in Figs. 6. Comparison of the development cycle of the cavitation cloud can be seen that the development time of the cavitation cloud under the condition of 15 MPa is the shortest and the cycle is smaller.

The computationally stabilised transient results were time-averaged to obtain the maximum velocity at the core surface, the maximum gas-phase volume fraction and the maximum pressure value at the wall under each pressure condition, as shown in Table 2. The maximum velocity value and the maximum pressure value at the wall surface increase with the increase of pressure, while the gas phase volume fraction at 15 MPa is lower than that at 12 MPa, which can be seen that the increase of pressure under the low pressure condition promotes the development of the cavitation cloud, and after a certain value is reached, due to the size of the flow field and the spatial limitation of the cavitation cloud development, the increase of pressure accelerates the development of the cavitation cloud, and the underdeveloped cavitation cloud quickly hits the wall, making the cavitation cloud gas-phase volume fraction and the period of the development of the cavitation cloud become smaller. Comparing the four inlet pressure conditions, a pressure value of 12 MPa is chosen as the inlet boundary condition to investigate the flow field characteristics of rotating cavitation water jets.
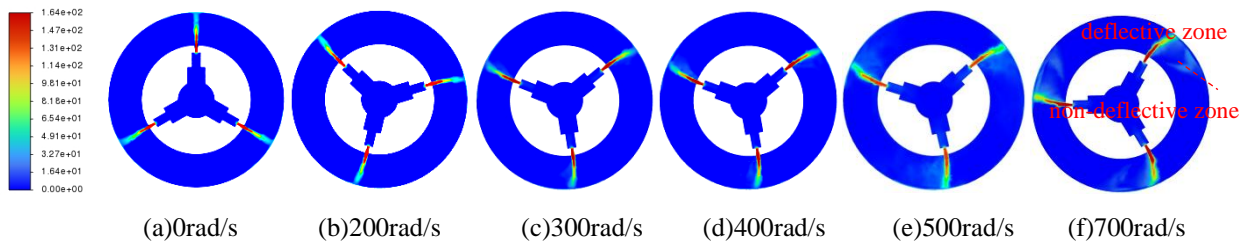
(a)0rad/s    (b)200rad/s    (c)300rad/s    (d)400rad/s    (e)500rad/s    (f)700rad/s

**Fig. 7 Comparison of velocity cloud images at different rotational speeds**



(a)0rad/s      (b)200rad/s      (c)300rad/s

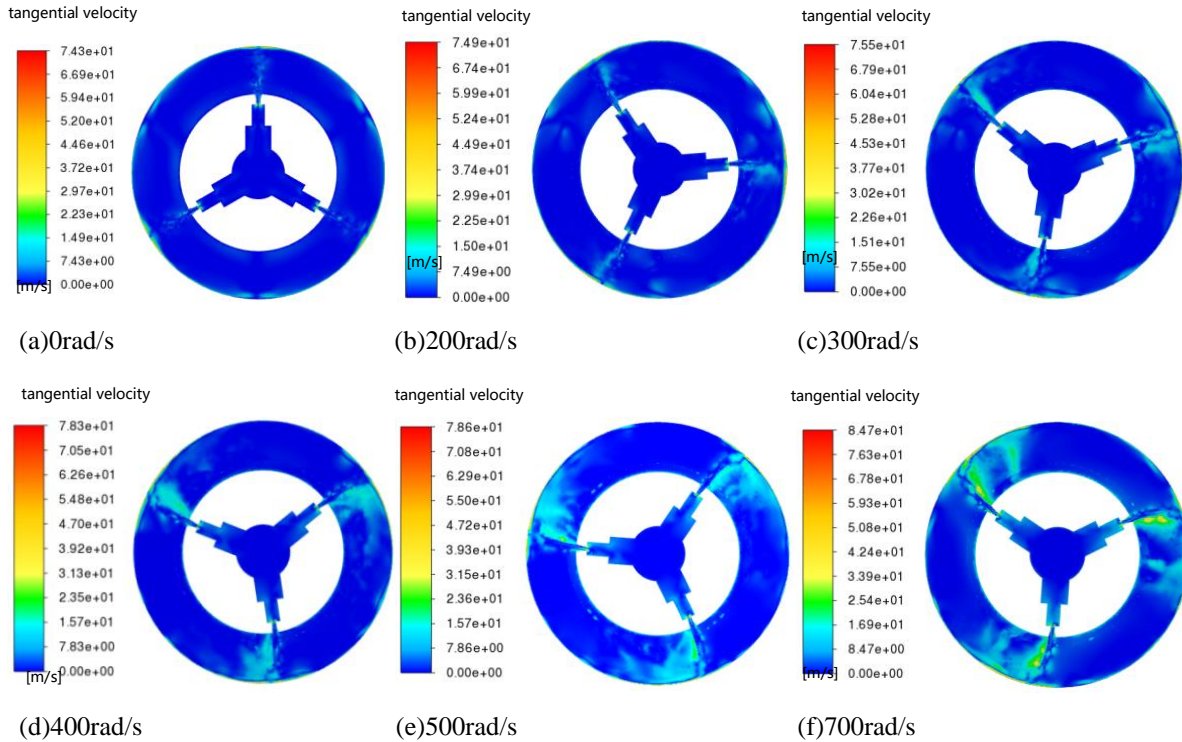(d)400rad/s      (e)500rad/s      (f)700rad/s

**Fig. 8 Comparison of tangential velocity cloud image at different rotational speeds**

## 4. 2 Analysis of Jet Velocity Field at Different Rotational Speeds

The rotary nozzle inlet pressure was set at 12 MPa. To clarify the velocity field characteristics and vortex characteristics of the rotating cavitation nozzle at different rotational speeds, the velocity clouds and tangential velocity clouds on the core surface of the nozzle jet were comparatively analysed at 0 rad/s, 200 rad/s, 300 rad/s, 400 rad/s, 500 rad/s, and 700 rad/s rotational speeds. It was found that as the rotational speed increases, the end of the jet is deflected to varying degrees, and a higher rotational speed leads to a more pronounced deflection phenomenon. At the same time, three pairs of vortices appear in the flow field varying with rotational speed and jet development, as depicted in Figs 7, 8, and 9.

Figure 7 shows the comparison of velocity clouds at different rotational speeds, which are analysed: The velocity flow field distributions of rotating cavitation jets have similar development trends. During the injection of the jet from the nozzle into the stationary flow field with both axial and tangential velocities, the time for the jet to develop along the tangential direction is short. The small tangential upward displacement under low rotational

speed conditions has a reduced impact on the jet flow trends, resulting in no apparent deflection of the main jet beam. The jet velocity was highest in the cylindrical and diffusion sections. The jet gradually moved downwards with a decreasing velocity, and after a small change still hits the cylindrical wall at a relatively high velocity. The main jet beam profile was slightly affected by increasing the rotational speed, and the tangential velocity dominated this slight variation. The maximum velocity of the main jet beam was not significantly changed. Still, the tangential velocity kept increasing, resulting in the existence of two parts of the jet, namely the deflection zone and the non-deflection zone, as shown in Fig. 7(f). When the rotational speed was increased to 700 rad/s, jet particles were developed most violently in the direction of tangential velocity. Furthermore, the tangential velocity was larger, the contour of the tangential velocity cloud in the flow field was gradually clearer, and the range of occupancy was expanding (Fig. 8). The deflection of the jet was more and more pronounced, and the tangential displacement of the jet was greater at a fixed time, making the erosion area of the wall larger.
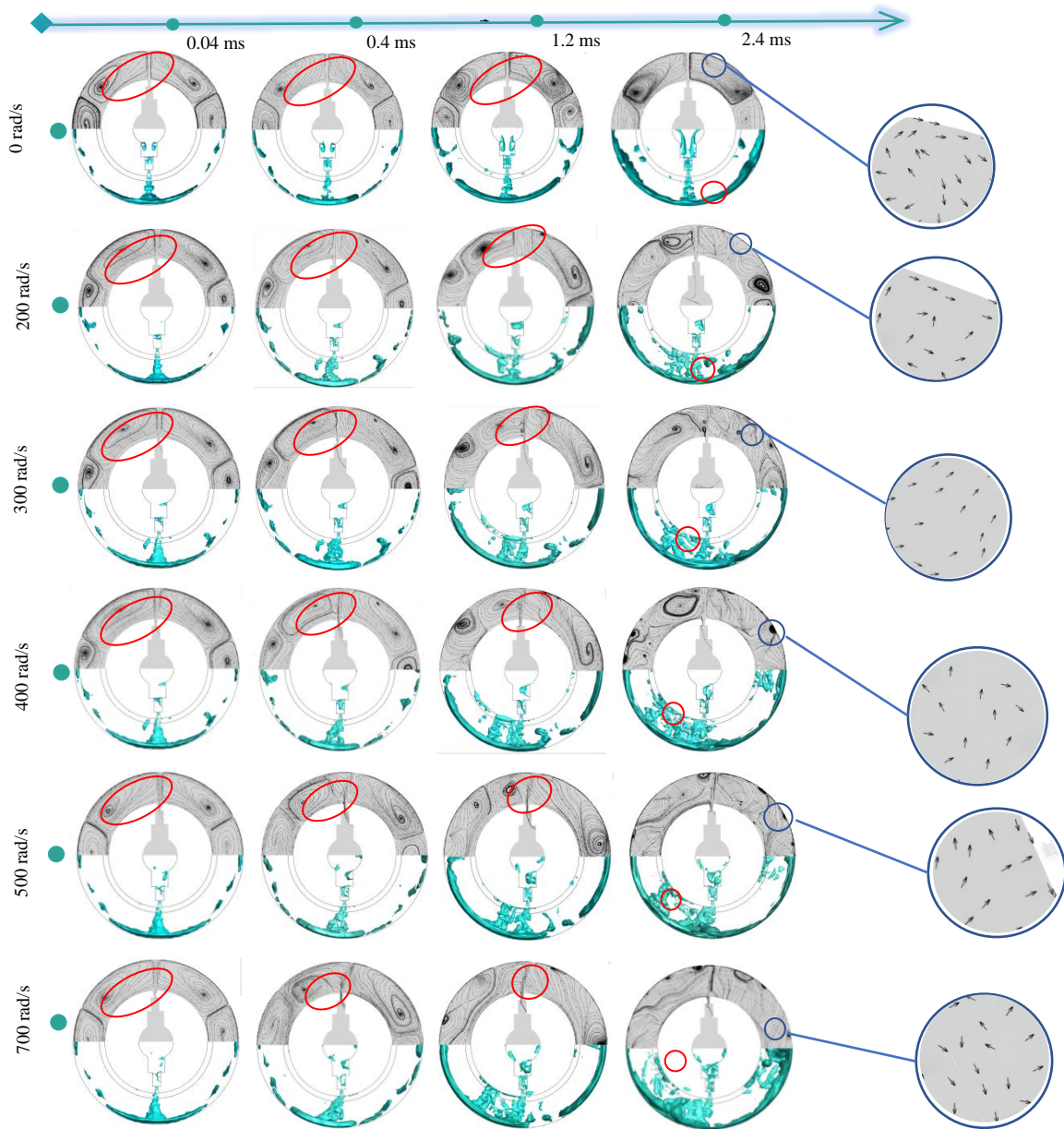
**Fig. 9 Plot of temporal development of vortex, velocity vectors and streamlines at different rotational speeds**

Figure 9 displays streamlines and vortex volumes splice plots at different rotational speeds. After analysing the flow form of the jet, it can be learnt that the jet ejected from the nozzle collides with the wall and then develops along the wall in two directions, one of which is the same as the rotational velocity and the other opposite to it. As can be observed from the jet development pattern diagram, the rotating jet is mainly controlled by the radial shear when it first enters the external flow field. At this time, the flow field in the shear layer velocity direction and the direction of the jet are opposite, which leads to the formation of two pairs of vortex rings. The three nozzles will form six pairs of vortex rings. A plot of the vortex evolution tracking one of the nozzles is presented in Fig. 9. After identifying the vortex structure using the Q-criterion, the evolution of the rotating jet vortex was classified into three phases: Developmental phase, excessive phase, and rotationally unstable phase. As the jet advances, the rotational instability increases, and the influence of the vortex structure gradually expands. Upon entering the rotational instability stage, the vortex ring mimicry decreases, and the large-scale vortex structure breaks down. With increasing the rotational speed, more fluid converges downstream of the jet outflow field, being affected by the tangential velocity. Larger tangential velocities and increased flow instability downstream lead to a change in the size difference between the two vortex rings. A larger rotation speed induces a more pronounced size difference, which increases the shear force of the fluid flow and promotes the generation of cavitation bubbles.
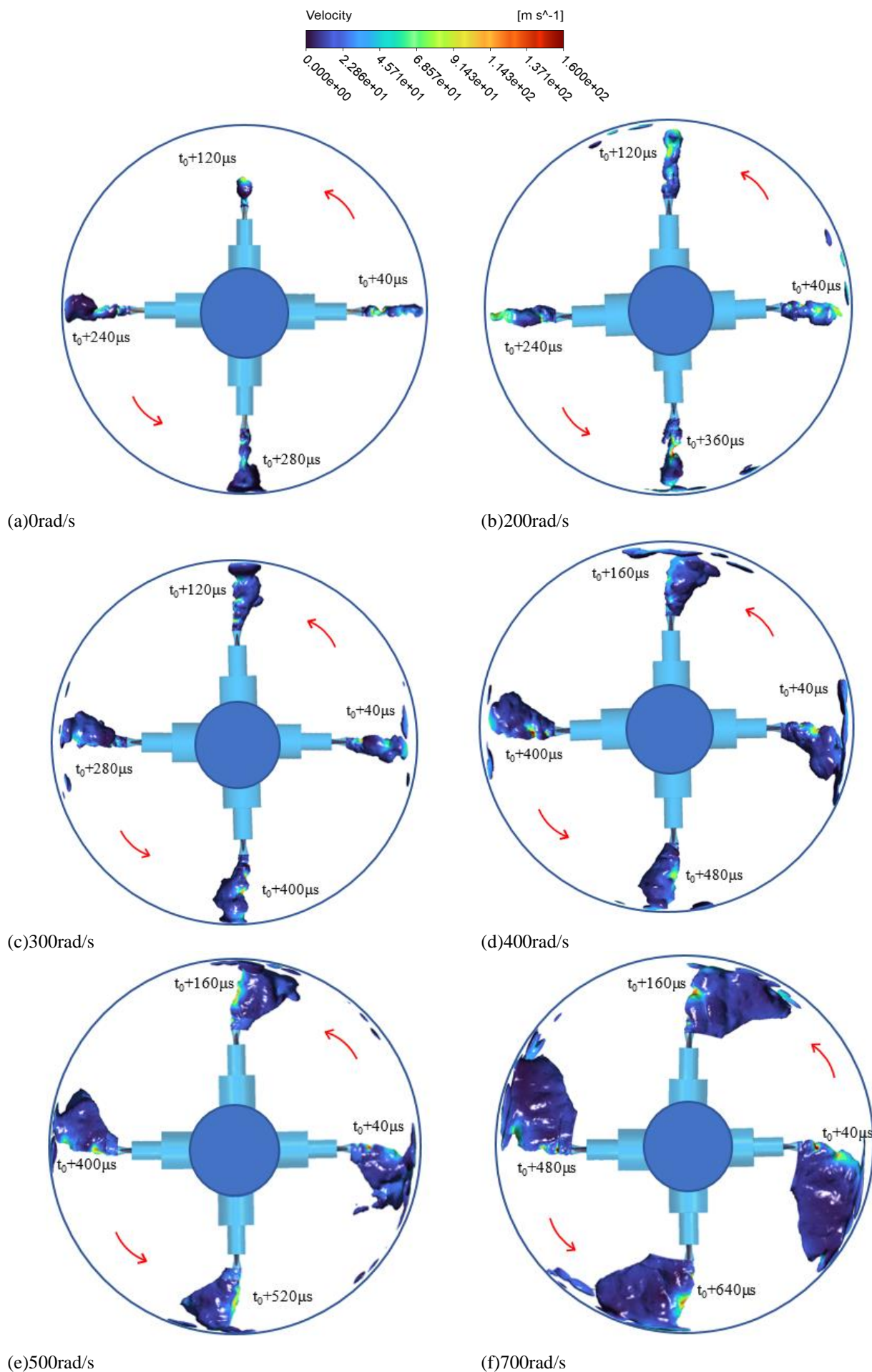
**Fig. 10 Cavitation cloud development diagram at different rotational speeds**

## 4. 3 Analysis of Cavitation Cloud Development Patterns at Different Rotational Speeds

The collapse of bubbles from cavitation is the key to descaling using cavitation jets. The effectiveness of cavitation directly affects the efficiency of cavitation jet descaling. The development period of the cavitation cloud, its morphological characteristics, and its collapse location are important characteristic parameters for describing the effect of cavitation. The cavitation cloud development patterns generated by nozzles rotating at 0 rad/s, 200 rad/s, 300 rad/s, 400 rad/s, 500 rad/s, and 700 rad/s at 12 MPa were simulated (as shown in Fig. 10). Typical positional maps of cavitation cloud development coloured by velocity in one cycle under different rotational speed conditions. The four phases of cavitation cloud development and evolution were also analysed: incipient, developmental, shedding, and collapse at different rotational speeds.

Figure 10(a) shows a plot of the position of the cavitation cloud development for one cycle when the nozzle is at rest. Three velocity peaks in the development of the cavitation cloud, and four distinct phases can be clearly seen in the figure. The development cycle of the cavitation cloud under this condition was about 280 μs. The cavitation cloud was small in size, and the cavitation cloud broke up upon contact with the wall. The cavitation bubbles were initiated in the cylindrical and diffusion segments and underwent a developmental phase with localized velocity fluctuations as they collapsed at the wall. The cavitation cloud development at a rotational speed of 200 rad/s was similar to that at 0 rad/s, and the four stages of development can be observed. The cavitation cloud was generated at $t_0+40$ μs, underwent shedding after 80 μs of development and enlargement, and began to collapse after $t_0+240$ μs, as depicted in Fig. 10(b).

Figure 10(e) shows the development of the 500 rad/s cavitation cloud, and there are only three developmental stages of the cavitation cloud under this condition: incipient, developing, and collapsing (no shedding stage). The cavitation cloud was generated at $t_0+40$ μs and began to collapse at $t_0+400$ μs after 360 μs of development and enlargement. The cavitation cloud was larger in size compared to the cavitation cloud development pattern under low rotational speed conditions. After the collision with the wall some of the bubbles collapse and the rest of the bubbles move along the wall under the action of the nozzle rotation. The latter results in a larger area of final action on the wall and the development of a longer period of about 520 μs.

At 700 rad/s, the developmental phase occupies a longer time and the volume of the cavitation cloud further increases. The cavitation cloud is in the form of a mass and behaves as a whole moving forward with the rotation of the nozzle when the area acting on the wall is the largest, and the development cycle is the longest. A comparison of the development cycle variation at each speed is illustrated in Fig. 11. When the rotational speed increases, the tangential velocity increases and the tangential displacement becomes larger. The cavitation cloud has enough time and space to develop in the direction of the tangential velocity, so both the maximum vapour phase
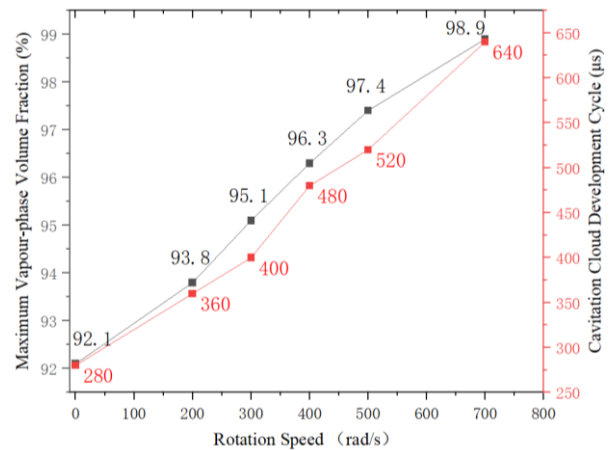


**Fig. 11 Line chart of maximum vapour phase volume fraction and cavitation cloud development cycle at different rotational speeds**

volume fraction and the period of cavitation cloud development increase with increasing rotational speed.

### 4.4 Wall Pressure Analysis at Different Rotational Speeds

To explore the impact of different rotational speeds on the pressure on the wall surface of the rotating cavitation jet, the variables were set to rotational speeds: 0, 200, 300, 400, 500, and 700 rad/s respectively. In the computational simulation, the inlet pressure was 12 MPa, and the following figure shows the pressure distribution of the rotating jet outer wall planar expansion at different rotational speeds.

As can be seen from the figure, the overall wall pressure distribution law at different speeds has obvious consistency, the nozzle rotates counterclockwise. As shown in the figure below from the right to the left, the fluid reaches the impact of the wall, the wall appears in three local areas like a circular high pressure point, the nozzle moves forward. The mass-like cavitation cloud collapses to form a negative pressure zone, and the distribution of the negative pressure zone exhibits water ripples with a band as shown in Fig. 12. With the increase in the rotational speed, the maximum pressure on the wall surface increases and then decreases. The negative pressure band has a tendency to move forward with the forward movement of the cavitation cloud. According to Fig. 13, when the rotational speed increases from 0 rad/s to 200 rad/s, the maximum pressure on the wall increases from 3.5 MPa to 4.9 MPa. The pressure change is obvious, the negative pressure band forms rounded water ripples spreading outward, compared with the high speed, and the high pressure zone acting on the wall is smaller under the condition of low rotational speed (as shown in Figs 12 a, b). When the rotational speed continues to increase, the maximum pressure on the wall starts to decrease. The maximum pressure on the wall began to fall. Particularly, at 300 rad/s when the pressure fell to 3.42 MPa, the average pressure value fell by 0.81 MPa. At this time, the pressure drop was the largest, more than 300 rad/s, the pressure drop slowed down to 700 rad/s, and the maximum pressure fell to 3.1 MPa. The average pressure value acting

on the wall tended to stabilise, and the high pressure zone around the negative pressure band moved forward. In parallel, the negative pressure band becomes longer (as shown in Figs 12 c, d, e, f).
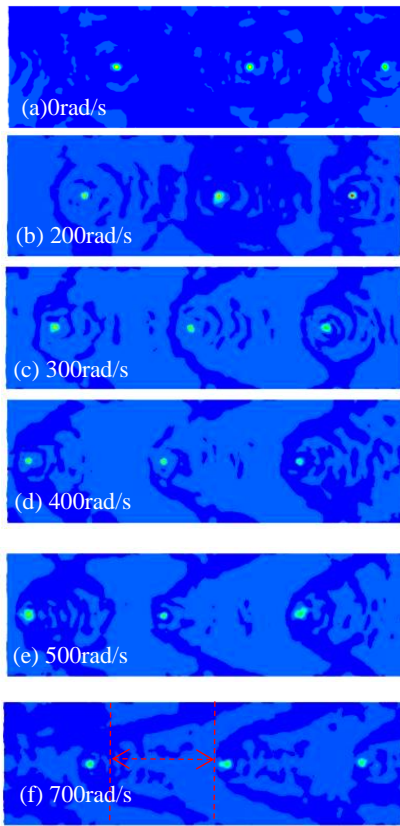


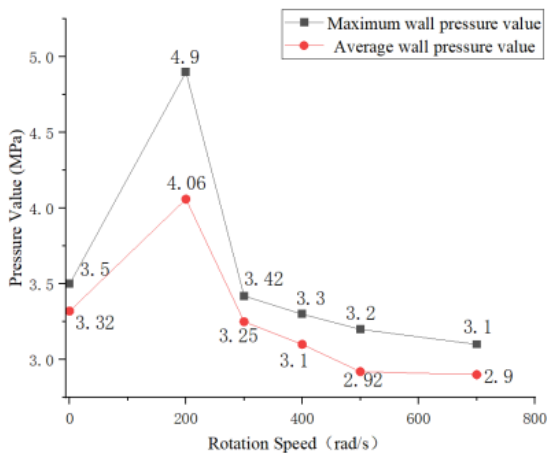**Fig. 12 Comparison of the wall pressure at different rotational speeds**



**Fig. 13 Comparison of the maximum pressure and average pressure of the jet acting on the wall at different rotational speeds, folded line graph**

### 4. 5 Comparison of Jet Fitting Curves at Different Rotational Speeds

The acquired numerical simulation results based on rotating nozzles at various speeds and the jet morphology of the individual nozzles of the rotating nozzle on the core

surface of the jet are plotted, as shown in Fig. 14 below. The core curve of the jet can be defined as $L$; the most terminal sample point of the core curve of the jet is $w$, the tangent line at the sample point $w$ is the straight line $a$, and the angle between the tangent line and the horizontal line is the impact angle $\alpha$; the line connecting the sample point $w$ and the starting point of the jet is the straight line $b$, and the angle between this straight line and the horizontal line is the deflection angle $\beta$.
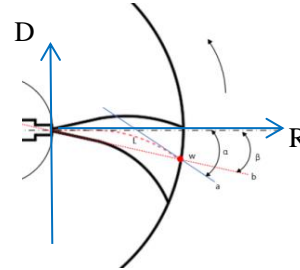


**Fig. 14 Schematic diagram of the jet morphology of a single nozzle**

The velocity maximum points for arcs of different radii on the core surface of the jet were extracted. Scatter-plots were plotted according to the coordinates of the position of each point as in Figs 15(a, b, c, d, e, f, g, h), and the jet maximum velocity flow curve was fitted according to the scatter-plot. At the initial position, the jet is not deflected. As the radius increases, the deflection distance of the fitted curve shows a parabolic growth trend as a function of growth:

$$D = L_0 + B_1 \cdot R + B_2 \cdot R^2 \tag{17}$$

In the above equation, $D$ is the jet deflection distance, $R$ refers to the jet distance, and $L_0$, $B_1$, and $B_2$ are the coefficients of the fitted equation.

The tangency function at point $w$ is as follows:

$$A = \alpha_0 + A_0 \cdot R \tag{18}$$

$A_0$ is the slope of the tangent line at point $w$. $A$ and $\alpha_0$ stand for the coefficients of the equation of the tangent line at point $w$.

The parameters of the distribution function of the fitted curve and the tangent function at point $w$ are presented in Table 3. As can be seen in Fig. 15, the pink bars show that the confidence interval is 95%, and the sample points are within or on the edge of the confidence band, which shows that the fitting function is more accurate. When the nozzle is in a stationary condition, the jet is continuously developed. The deflection distance between the start point and the point $w$ is zero during the arrival at the wall. The jet deflection angle and the jet impact angle do not change; they are both 0°. When the nozzle rotates counterclockwise at a certain speed, the dimensionless deflection distance, the jet deflection angle, and the jet impact angle increase with the increase of the radius. The value of the deflection distance, the jet deflection angle, and the jet impact angle are maximum at point $w$.
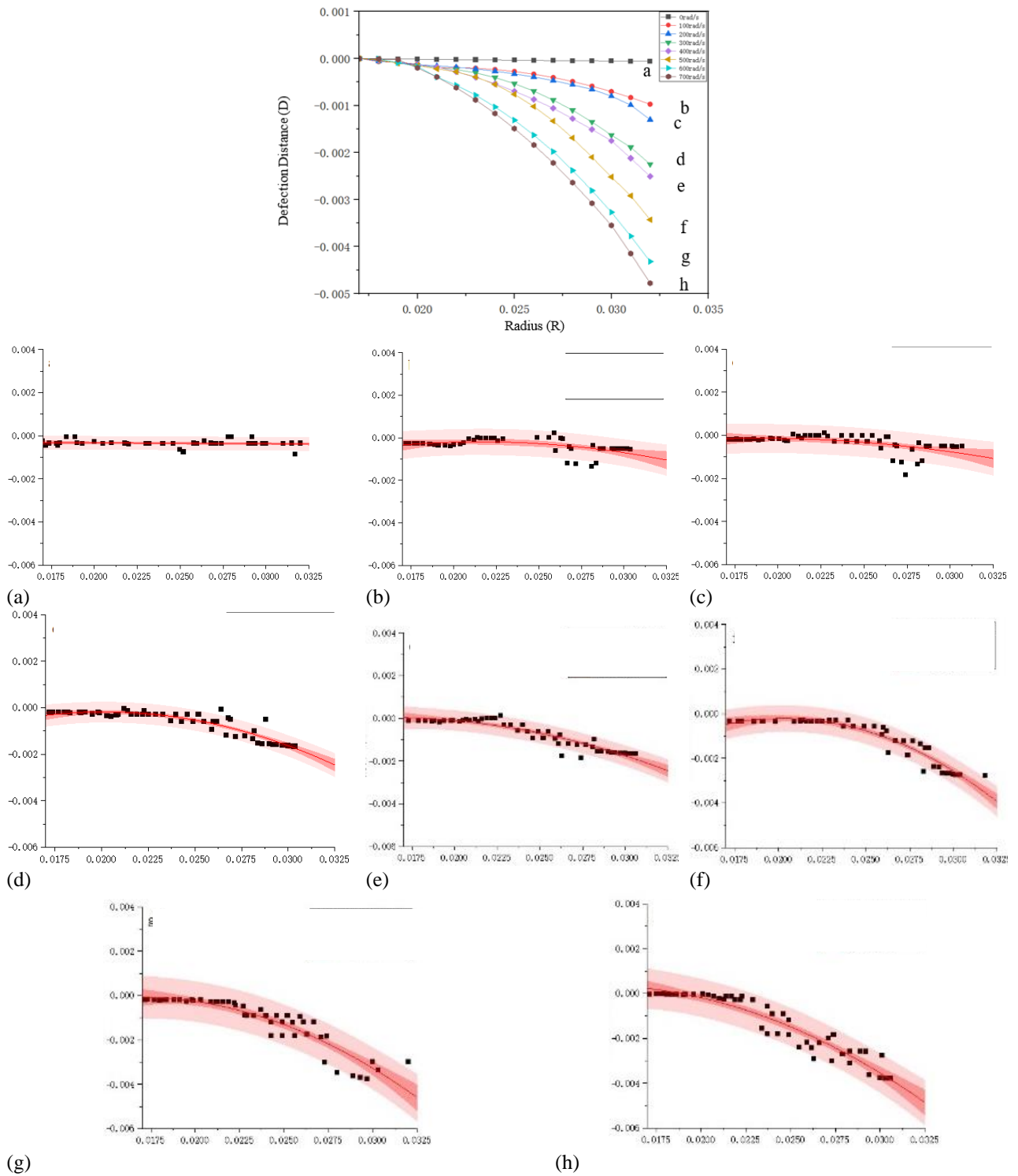
(a)    (b)    (c)

(d)    (e)    (f)

(g)    (h)

**Fig. 15 Summary and comparison of the jet fitting curves**

**Table 3 Summary of parameters of the jet fitting curve**

|  | $\alpha_0$ (×10⁻⁵) | $A_0$ (×10⁻³) | $L_0$ (×10⁻⁴) | $B_1$ (×10⁻³) | $B_2$ | $\alpha$, $^\bullet$ |
|---|---|---|---|---|---|---|
| 0 | 4.31 | -3.28 | 1.02 | -7.04 | 5.98×10⁻² | 0 |
| 100 | 0.0358 | -0.0142 | -0.129 | 0.0141 | -4.05 | 8.1 |
| 200 | 0.0861 | -0.031 | -0.21 | 0.022 | -5.97 | 17.2 |
| 300 | 0.0927 | -0.036 | -0.398 | 0.0427 | -11.61 | 19.8 |
| 400 | 0.0997 | -0.039 | -0.35 | 0.0396 | -11.33 | 21.3 |
| 500 | 0.00129 | -0.051 | -0.656 | 0.0701 | -18.83 | 27.03 |
| 600 | 0.0013 | -0.054 | -0.459 | 0.0568 | -17.49 | 28.37 |
| 700 | 0.00154 | -0.063 | -0.462 | 0.0591 | -18.57 | 32.2 |

Figure 15 shows a summary comparison of the fitted curves of the jet at different rotational speeds. Each of the jet fitting curves from 0 rad/s to 700 rad/s can be clearly seen in the figure. As the rotational speed increases, the value of the deflection distance at point w, the deflection angle of a jet, and the jet impingement angle keep increasing. The near-wall tangent slope $A_0$ and jet impingement angle $\alpha$ presented by the fitted jet curve are listed in Tab. 3 above, and the fitted jet impingement angle functions are:

$$\alpha = 1.16417 + 0.07439 \cdot x - 0.000045286 \cdot x^2 \qquad (19)$$

where $x$ is the nozzle rotation speed and $\alpha$ denotes the jet impingement angle. The fitted function, based on the rotational speed, predicts the corresponding impact angle of the jet to the wall. It provides a reference for the design of the rotating nozzle angle.

## 5. CONCLUSION

This work simplified the geometry of the cavitation water jet nozzles with rotational characteristics, and the Large Eddy Simulation and the WALE model were used to simulate the development of cavitation clouds for different inlet pressure. It is found that the cavitation effect is first enhanced and then weakened with the increase of pressure. By analysing and comparing and tangential velocity cloud diagrams of the internal flow field of the rotating cavitation water jet, the streamline and vorticity collocation diagrams, the cavitation cloud unfolding diagrams, as well as the jet fitting curve functions at different rotational velocities:

With the gradual increase in the rotational speed, the end of the jet is deflected to varying degrees. Under low rotational speed conditions, the jet exhibits no deflection. When the rotational speed continues to increase, the tangential velocity increases, the tangential displacement increases, and the deflection becomes more pronounced. Three pairs of six larger vortices exist on the core surface of the initial jet development, formed by the collision of the jet with the wall after the collision of the two streams of fluid. Being affected by the shear effect, with the increase in the rotational speed, the large vortex structure gradually breaks up and separates into small vortices during the development of the jet. At 700 rad/s, the large vortex structure is completely disappeared.

In this work, the maximum vapour phase volume fraction of the cavitation cloud and the period of cavitation cloud development were found to be proportional to the rotational velocity. When the rotational speed increases, the developmental phase occupies a longer time, and the volume of the cavitation cloud becomes larger. Nonetheless, when the rotational speed is too high, there is no shedding phase, the time of jet flow grows, and the cavitation cloud is allowed to fully develop.

At lower rotational speeds rotational speed on the wall pressure to promote the role of rotational speed when the rotational speed reaches a certain value of rotational speed on the increase in wall pressure to inhibit, that is, the nozzle rotational speed on the wall pressure of the impact of the pressure of the jet with the increase in the pressure of the weakening. There are three localised areas of circular high pressure standing points on the wall surface. As the nozzle rotates, the high rotational speed has a stronger impact on the diffusion of high pressure covering points on the wall surface, and the resulting negative pressure band is significantly grown.

The fitted development curve for the core area of the jet can better reproduce the development of the core area of the jet, with no shift in the fitted jet curve at 0 rad/s. With increasing the rotation speed, the jet is deflected to different degrees. At a distance farther away from the nozzle outlet, the deflection phenomenon is more obvious. The curvature of the fitted curve is also positively correlated with the jet velocity. A larger rotational speed leads to a bigger jet deflection distance, deflection angle, and impact angle at the near-wall, and the operational performance of the pipeline is greatly affected.

## CONFLICT OF INTEREST

The authors hereby declare that the content researched in this paper does not infringe on the intellectual property rights of others and that there are no intellectual property disputes and conflicts of interest.

## AUTHORS CONTRIBUTION

**W. Wu:** conceptualization, methodology, software; **Y. Xu:** data curation, writing-original draft preparation, investigation; **Y. Yan:** validation, investigation; **S. L:** supervision; **J. Zhang:** software; **Z. Wang:** writing-reviewing and editing.

## REFERENCES

Bensow, R. E., & Bark, G. (2010). Implicit LES predictions of the cavitating flow on a propeller. *Journal of Fluids Engineering, 132* (4), 041302. https://doi.org/10.1115/1.4001342

Bhatt, M., & Mahesh, K. (2019). Numerical investigation of partial cavitation regimes over a wedge using large eddy simulation. *International Journal of Multiphase Flow, 122*, 103155. https://doi.org/10.1016/j.ijmultiphaseflow.2019.103155

Cai, T. F., Pan, Y., & Ma, F. (2020). Effects of nozzle lip geometry on the cavitation erosion characteristics of self-excited cavitating waterjet. *Experimental Thermal and Fluid Science*, *117* https://doi.org/10.1016/j.expthermflusci.2020.110137Get rights and content

Dabiri, S., Sirignano, W. A., & Joseph, D. D. (2010).

Interaction between a cavitation bubble and shear flow. *Journal of Fluid Mechanics, 651*, 93-116. https://doi.org/10.1017/S0022112009994058

Guo, Q., Zhou, L. J., Wang, Z. W., & Cheng, H. (2018). Numerical simulation for the tip leakage vortex cavitation. *Ocean Engineering, 151*(3), 117-127. https://doi.org/10.1016/j.oceaneng.2017.12.057

Ji, B., Long, Y., & Long, X. P. (2017). Large eddy simulation of turbulent attached cavitating flow with special emphasis on large scale structures of the hydrofoil wake and turbulence-cavitation interactions. *Journal of Hydrodynamics, 29*(1), 27-39. https://doi.org/10.1016/S1001-6058(16)60715-1

Chen, J. X., Yang, R. Y., Huang, Z. W., Li, G. S., Qin, X. Z., Li, J. B., & Wu, X. G. (2022). Detached eddy simulation on the structure of swirling jet flow field. *Petroleum Exploration and Development, 49*(4), 929-941. https://doi.org/10.1016/S1876-3804(22)60322-7

Li, D. Y., Zhao, M. S., Zeng, Q. F., Zheng, Z. Y., Pei, Y. U., Yao, S. Y., & Yao, L. M. (2023). Numerical simulation analysis of hydrodynamic characteristics of modified wedge blade rotary cavitator. *Chinese Ship Research*, (01), 181-188. https://doi.org/10.19693/j.issn.1673-3185.02547

Ni, L. (2022). *Hydrodynamic analysis of rotating descaling nozzle for ultra high pressure water jet ship* [Master's Thesis, Zhejiang Ocean University]. https://doi.org/10.27747/d.cnki.gzjhy.2021.000098

Peng, C., Tian, S., & Li, G. (2018). Joint experiments of cavitation jet: High-speed visualization and erosion test. *Ocean Engineering, 149*, 1-13. https://doi.org/10.1016/j.oceaneng.2017.11.009

Smagorinsky, J. (1963). General circulation experiments with the primitive equations: I the basic experiment. *Monthly Weather Review, 91*(3), https://doi.org/10.1175/15200493(1963)091x0003C;0099:gcewtp>2.3.co;2

Wang, J. X., Wang, Z. C., Xu, Y., Zhang, J. L., & Li, S. (2023a). Experimental study on the performance of rotary self-feeding cavitation jet nozzle and oil pipe descaling. *Mechanical Science and Technology, 1-10*. https://doi.org/10.13433/j.cnki.1003-8728.20230048

Wang, L. A., Xu, Y., Wang, Z. C., Li, S., Zhang, J. L., & Liu, H. S. (2023b). Large eddy simulation of cavitation water jet flow field in organ-pipe nozzle. *Mechanical Science and Technology*, 1-10. https://doi.org/10.13433/j.cnki.1003-8728.20230072

Wang, R. H., Zhou, W. D., Shen, Z. H., & Yang, Y. Y. (1999). Study on the mechanism of rotary jet rock-breaking drilling. *Chinese Journal of Safety Science*, (S1), 59+104. https://doi.org/10.16265/j.cnki.issn1003-3033.1999.s1.001

Wang, G., & Ostoja-Starzewski, M. (2005). Large eddy simulation of a sheet/cloud cavitation on a NACA0015 hydrofoil. *Applied Mathematical Modelling, 31*(3), 417-447. https://doi.org/10.1016/j.apm.2005.11.019

Wu, X. Y., Zhang, Y. Q., Tan, Y. W., Li, G. S., Peng, K. W., & Zhang, B. (2022). Flow-visualization and numerical investigation on the optimum design of cavitating jet nozzle. *Petroleum Science*, (05), 2284-2296. https://doi.org/10.1016/J.PETSCI.2022.05.016

Xu, H. B. (2022). Research on optimal design of new hydraulic cavitation tool [D]. Xi'an Petroleum University, 2022. https://doi.org/10.27400/d.cnki.gxasc.2022.000166.

Yu, A., Feng, W., & Tang, Q. (2022). Large eddy simulation of the cavitating flow around a clark-y mini cascade with an insight on the cavitation-vortex interaction. *Ocean Engineering*, https://doi.org/10.1016/j.oceaneng.2022.112852

Zhao, J., Jiang, E. Y., Qi, H., Ji, S. M., & Chen, Z. Z. (2020). A novel polishing method for single-crystal silicon using the cavitation rotary abrasive flow. *Precision Engineering, 61*, 72-81. https://doi.org/10.1016/j.precisioneng.2019.10.002

Zhao, J., Liao, H. L., Xu, Y. J., Shi, F. X., Sun, B. J., Chang, F. R., & Han, X. Q. (2023). Experimental and theoretical evaluation of tubing cutting with rotating particle jet in oil and gas borehole operation. *Energy, 282*, 128468. https://doi.org/10.1016/j.energy.2023.128468